Arabian Journal of Chemistry (2023) **16**, 104703

King Saud University

Arabian Journal of Chemistry

www.ksu.edu.sa
www.sciencedirect.com

ORIGINAL ARTICLE

Phytogenic fabrication of iron oxide nanoparticles and evaluation of their *in vitro* antibacterial and cytotoxic activity

Sheik Aliya [a], Muruganantham Rethinasabapathy [a], Jingon Yoo [a], Eunsu Kim [a], Joo-Yoon Chung [b], Jong-Ho Cha [b,c,*], Yun Suk Huh [a,*]

[a] *NanoBio High-Tech Materials Research Center, Department of Biological Sciences and Bioengineering, Inha University, Incheon, Republic of Korea*
[b] *Department of Biomedical Sciences, College of Medicine, Inha University, Incheon, Republic of Korea*
[c] *Department of Biomedical Science and Engineering, Graduate School, Inha University, Incheon, Republic of Korea*

Received 6 October 2022; accepted 19 February 2023
Available online 23 February 2023

KEYWORDS

Antibacterial;
Antioxidant;
Cytotoxic activity;
Iron oxide nanoparticles;
Nigella sativa

Abstract Several metal-based nanoparticles (NPs) have been found to be toxic and are known to exert adverse health outcomes with irreversible side effects. This highlights the need to discover effective, stable, and biocompatible therapeutic components using natural sources. Here, a hexane extract of *Nigella sativa* seeds was used to synthesize iron oxide NPs (NS-IONPs) embedded with *N. sativa* phytoconstituents. The extract acted as a reducing agent that restricted the size of the NS-IONPs to 5–6 nm, signifying the potential to be cleared through the renal system. The fabricated NS-IONPs had a prominent effect on pathogenic gram-negative bacteria, *E. coli* (19.3 mm) and *Salmonella typhi* (14.2 mm) and lung cancer cells (lowest IC_{50} of 18.75 µg/mL) mainly by binding to the phospholipid components of the cell membrane. This resulted in cell shrinkage and further inhibited cell growth. Transmission electron microscopy analyses revealed that the mechanisms of cellular NP uptake varied depending on the cell type. Accumulation of NS-IONPs inside the cell increased BAX expression and arrested the cells at the G0/G1 phase, thereby conspicuously extending the G0 phase to initiate necrosis. Thus, these finding suggest that the synthesized NS-IONPs exhibited high antibacterial activity and effective cytotoxicity against cancer cell lines A549 and HCT116 compared to IONPs. The innovation of the current study is that the biogenic fabrication of IONPs is simple and

---

* Corresponding authors.
E-mail addresses: chajongho@inha.ac.kr (J.-H. Cha), yunsuk.huh@inha.ac.kr (Y.S. Huh).

Peer review under responsibility of King Saud University.

Production and hosting by Elsevier

https://doi.org/10.1016/j.arabjc.2023.104703

cost effective results in stable nanomaterial, NS-IONPs with potential antibacterial and anticancer activity, which can be explored furthermore for various biomedical applications.

1. Introduction

To date, several types of nanoparticles (NPs; defined as particles 1–100 nm in diameter) have been designed and are employed in a wide variety of fields, including electronics, cosmetics, food, environmental analysis, paint and dye remediation, and biomedicine (Stark et al., 2015). Their small size greatly increases their surface area, rendering them highly reactive and tunable. Nanostructures can be fabricated using chemical, physical, and biological methods. Biological approaches and simple bio-reduction methods are generally preferred to avoid the toxicity and detrimental effects of the chemicals (e.g., capping agents, reducing agents, and solvents) used to synthesize NPs (Augustine et al., 2020).

Recently, magnetic iron oxide NPs (IONPs) have garnered increasing attention due to their unique physicochemical properties, low cost, and low toxicity. IONPs have been extensively studied due to their magnetic properties (Noqta et al., 2019) and have been widely employed in the treatment of contaminated industrial sites, as well as in the fabrication of nanowires, textiles, plastics, nanofiber coatings (nano.gov), and tissue repair, in addition to biological fluid detoxification, immunoassays, cell separation, and drug delivery (Mortimer and C.j., 2017). However, their size has been a major limitation for medical applications. Biologically synthesized IONPs with a diameter of 10–100 nm have been used as an effective tool in medical diagnosis and the treatment of diseases such as cancer (Byun et al., 2022). Particularly, magnetic IONPs have been employed in targeted drug delivery by applying an external magnetic field to rapidly deliver a drug to a specific target site. These NPs have attracted increasing interest in the field of biomedicine due to their high efficiency, low toxicity, small size, rapid diffusion into human tissue, low dipole–dipole interaction, high surface area for the attachment of therapeutic drugs, and low deposition rate (Ayyanaar et al., 2020).

Cancer, a disease accounting for major causes of death globally. Every year, approximately 4 lakh children are diagnosed with this dreadful disease. This has impacted on the peoples' mental health as well as their social life. Bacterial infections are another major cause of death of the cancer patients in hospitals. Drugs that are currently on the market causes adverse side effects (Sung et al., 2020). Therefore, it is necessary to find novel therapeutic compounds from natural resources that have improved efficacy without causing side effects. With the recent development and popularization of green synthesis approaches, various plant extracts have been used to synthesize plant based IONPs that are ecofriendly and functionally effective. Plant-based IONPs have been fabricated using *Rhamnella gilgitica* leaf extract (Iqbal et al., 2020); *Gardenia jasminoides* and *Lawsonia inermis* extracts (Naseem and M.a., 2015, 2015); *Skimmia laureola* (Alam et al., 2019); *Moringa oleifera* leaf extract (Aisida et al., 2020); *Ageratum conyzoides* root and leaf extracts (Madivoli et al., 2019); *Callistemon viminalis* floral extracts (Hassan et al., 2018), and *Eichhornia crassipes* leaf extract (Jagathesan and Rajiv, 2018). These extracts are reported to contain phytochemicals that act as reducing, capping, and/or stabilizing agents.

Here, we assessed the benefits of synthesizing IONPs using *Nigella sativa* seed extract. *N. sativa* (black cumin) is an annual medicinal herb of the Ranunculaceae family that is native to the Mediterranean region and is widely used to treat various diseases. This herb contains a wide variety of alkaloids, terpenoids, saponins, volatile oil, fatty acids, tannins, and other phytocomponents (Almatroudi et al., 2020). In turn, these bioactive components contain functional groups such as carboxyl, methyl, and hydroxyl groups, which may be responsible for the reduction of ferric ions to produce IONPs. These components bind to the surface of metal NPs, thus preventing aggregation and maintaining the stability of the NPs. The phytogenically fabricated IONPs using hexane extract of *N. sativa* seeds (NS-IONPs) are characterized using a variety of analytical methods. UV–vis spectrophotometry was used to study the optical properties of the NPs, powder X-ray diffraction (XRD) was used to analyze their structure, and X-ray photoelectron spectroscopy (XPS) was employed for surface chemical analysis. Additionally, Fourier-transform infrared (FTIR) spectroscopy was used to identify the functional groups present on the NPs, whereas XPS, scanning electron microscopy (SEM), EDX, high-resolution transmission electron microscopy (HR-TEM), and EDS were all used to evaluate the size, morphology, and surface characteristics of the NPs. The zeta potential of the NPs was also evaluated to provide insights into the processes that drive NP formation as well as their surface charges, which can be used to determine the binding efficiency of the NPs to a given target receptor. Finally, in this study, the antibacterial and anti-cancer properties of the NS-IONPs synthesized from hexane extract of *N. sativa* seeds were monitored *in vitro* to evaluate their therapeutic efficiency.

2. Materials and methods

2.1. Materials

Nigella sativa seeds were purchased from the Yangnyeongsi herbal medicine market, Seoul, South Korea. The seeds were washed, air dried for a week and stored at 4 °C in polythene container until further processing. Iron (III) chloride hexahydrate ($FeCl_3{\cdot}6H_2O$), iron (II) chloride tetrahydrate ($FeCl_2{\cdot}4H_2O$), commercial iron oxide nanoparticles and citric acid were purchased from Sigma-Aldrich, ammonium hydroxide solution (25 %–28 %) was purchased from Merck. All the chemicals were of analytical grade and all solutions used in the experiments were prepared using deionized water. Two gram-negative bacterial strains (*Escherichia coli* [ATCC 11775] and *Salmonella typhimurium* [ATCC 13311]) and a gram-positive strain (*Staphylococcus aureus* [ATCC 6538]) were used to determine the antibacterial activity of the commercial IONPs and NS-IONPs. The strains were all grown in nutrient agar medium obtained from Merck, cultured at 37 °C, and preserved in glycerol at − 80 °C until further analysis.

2.2. Preparation of the plant extract

To produce the seed extract, 5 g of *N. sativa* seeds were dried in an oven for 1 h and then ground into a fine powder. The powder was mixed with 50 mL of hexane and left for 2–3 h before being filtered through Whatman filter paper and stored at room temperature prior to use.

2.3. Synthesis of NS-IONPs using coprecipitation

IONPs were synthesized using a previously reported coprecipitation method (Deshmukh et al., 2019 (2019).) with slight modifications. $FeCl_3$-$6H_2O$ and $FeCl_2$-$4H_2O$ salts at a 2:1 M ratio was heated at 60 °C for 5 min. Approximately 20 mL of the hexane extract from the *N. sativa* seeds was added and the mixture was stirred for 2 h at room temperature. Ultrasonication was then conducted for 30 min with a probe sonicator (Sonics, Vibra-cell) at room temperature with an amplitude of 50 % and an on–off pulse of 50 and 10 s, respectively. During sonication, 50 mL of 25 %−28 % ammonia solution was added dropwise for approximately 30 min. The suspension was then allowed to react for another 30 min. A change in color confirmed the formation of NS-IONPs. Citric acid (0.02 mg/mL) was subsequently added to the suspension, followed by stirring for nearly 1 h at 500 rpm. The suspension was then centrifuged, and the resulting pellet was washed three times with deionized water. Finally, the magnetic NS-IONP pellet was dried in a vacuum at 60 °C for 12 h.

2.4. Characterization of the NS-IONPs

XRD (X'Pert PRO MRD diffractometer, Phillips) was used to analyze the structure of the IONPs, and XPS chemical analysis was conducted on an ESCALAB MK II X-ray spectrometer (Thermo Scientific). XPS is a powerful technique that allows for the characterization of the photoelectron spectrum of target compounds. An X-ray diffractometer was used to produce the X-ray spectrum (Whitfield and L., 2004). The peaks in the spectrum represent the characteristic kinetic energy of the electrons ejected by the atoms. The photoelectron peak energies and intensities enable the identification and quantification of all elements present on the surface of the IONPs except for hydrogen. FTIR spectroscopy (JASCO 6600, Bruker Corp, Germany) was used to identify the functional groups and biomolecules present in the IONPs. The functional groups in *N. sativa* extract responsible for the reduction of the ferric ions were identified over a 400 to 4000 cm^{-1} range at a resolution of 4 cm^{-1} at 25 °C. A UV–vis spectrophotometer (Jasco V-770) was used to analyze the optical properties of the IONPs and the hexane extract. Water and hexane were used as blank references for the respective samples. The samples were tested in a quartz cuvette, and the spectra were read at 200–700 nm. A dynamic light scatterer (DLS) (Photal Otsuka Electronics, Japan) was used to measure the mean diameter and size distribution of the NPs dispersed in deionized water. A zeta potential analyzer was also used to monitor the surface charge of the NPs, which is indicative of the stability of the NPs in a dispersion. The NPs were suspended in distilled water and sonicated for approximately 10 min. The morphology and size of the synthesized IONPs were characterized using SEM, EDS (Hitachi S-4300), and HR-TEM (CM200) images. The IONP samples were observed at a voltage of 20 kV with a frequency of 2838 cps. To produce a conductive sample, the slides were coated with a platinum layer. The prepared samples were analyzed at various resolutions and magnifications.

2.5. Biological activities

2.5.1. Antibacterial analysis

2.5.1.1. Antimicrobial assay. Antimicrobial assay was conducted using agar diffusion. The test organisms used for the assays were the gram-positive *S. aureus* and gram-negative *E. coli* and *S. typhi*. Mueller-Hinton agar (MHA) sterilized in an autoclave at 121 °C for 20 min was poured in a petri dish and solidified. Spread plates were then prepared by inoculating 100 μL of bacterial (1.5×10^{8} cells) culture. Inoculation is made with the broth culture grown overnight diluted to match 0.5 McFarland turbidity standard. Sterile paper discs (10 mm in diameter) were impregnated with tetracycline (10 μg/mL) as a positive control. NPs were then added to the medium and pre-incubated at room temperature for 1 h, followed by incubation at 37 °C for 24 h. The cytotoxicity of the samples for the target bacterial strain was visualized by monitoring and measuring the diameter of the inhibition zone around the paper discs.

2.5.1.2. Bacterial growth inhibitory assay. To examine the effect of NS-IONPs on microbial growth, *S. aureus*, *E. coli*, and *S. typhi* were individually grown overnight in 100 mL of MHA broth, 50 mL of which was supplemented with NS-IONPs at 50 μg/mL, whereas the controls were exposed to 50 mL of untreated medium. After 12 h, bacterial growth was assessed by measuring the absorbance at 600 nm using an ELISA plate reader (Varioskan^{TM} LUX multimode microplate reader).

2.5.1.3. Scanning electron microscopy. SEM analysis was conducted to observe the bactericidal activity of NPs on the surface of microorganism. NS-IONPs were inoculated into the growth media of the selected microorganisms and the cultures were incubated overnight. A non-treated culture was also prepared to serve as a control. The treated and untreated were then processed. First the culture was pelleted out by centrifuging at 2000 RPM for 5 min, the culture pellet was subjected to dehydration in 30 % ethanol followed by 50 %, 75 % and finally with 100 % ethanol. Again the culture was pelleted out by centrifuging at 2000 RPM for 5 min, vacuum dried at 60 °C for 4 h and then it was examined under SEM.

2.5.2. Anticancer activity of the synthesized NS-IONPs

2.5.2.1. Cell culture and cell line maintenance. Colorectal cancer cells (HCT116) and lung cancer cells (A549) were purchased from the American Type Culture Collection (ATCC, Manassas, USA). These cells were cultured in McCoy's 5A medium and RPMI-1640 medium, respectively, supplemented with 10 % (v/v) fetal bovine serum and a 1 % penicillin–streptomycin cocktail at 37 °C in a 5 % CO_2 incubator (Dariya et al., 2019).

2.5.2.2. Cell viability testing – CCK-8 assay. To assess the cytotoxic effects of NS-IONPs, the cancer cell lines HCT116 and A549 were incubated with various concentrations (1.56 to 100 μg/mL) of IONPs and NS-IONPs. After 24 h and 48 h of incubation, cell viability was measured using a CCK-8 cell counting kit following the manufacturer's instructions. IC_{50} values were determined using sigmoidal dose–response analysis.

2.5.2.3. Observation of cytomorphological changes. Cytomorphological changes were observed in the cancer cell lines HCT116 and A549 treated with various concentrations of NPs. After 48 h of incubation, the morphological changes in the cells were examined using bright-field microscopy. The media was removed, and the cells were washed with PBS and fixed for 15 min in 4 % paraformaldehyde. The cells were then treated with DAPI to stain their nuclei. Finally, the cells were observed under a fluorescent microscope (EVOS M7000, Invitrogen, Thermo Fisher Scientific).

2.5.2.4. SEM and TEM analysis of the cells. SEM equipped with a thin-window EDAX system for X-ray microanalysis was used to observe the morphological changes in the cancer cells. TEM analysis of the A549 cells was conducted after treatment with 50 μg/mL of NS-IONPs for 48 h. The samples were prepared for analysis as described in a previous study with slight modifications (De Berardis et al., 2010).

2.5.2.5. Viability assay. Calcein-AM and propidium iodide (PI) were used as viability stains. Working solutions of the stains were prepared by diluting the stocks in PBS. Assay solutions were prepared by diluting 1 μL Calcein-AM and 10 μL PI in 1 mL of PBS. The control and treated cells were grown on microscopic cover slips, after which they were washed twice with PBS then treated with 100 μL of assay solution and incubated for 20 min at 37 °C. After washing the cells, DAPI was added to stain the nuclei and the cells were incubated for 5 min. The cells were then washed and assessed using fluorescence microscopy (EVOS M7000 cell imaging system). Live and dead cells were simultaneously visualized using the double pass filter for fluorescein and Texas red. The cellular esterase of viable cells converted Calcein-AM acetoxymethyl ester into a green-fluorescent product. In contrast, the dead cells were permeable to PI, which bound to the chromatin and was observed as red fluorescence.

2.5.2.6. Clonogenicity assay. To perform the colony formation assay, colorectal cancer cells (HCT-116) and lung cancer cells (A549) were plated in 6-well plates at a density of 100 cells per well. The following day, the cell lines were treated with vehicle (water) and NS-IONPs at specified concentrations (50 & 100 μg/ml) for 48 h. The media were replenished after three days without re-treatment. After 12 days, the medium was removed, and cell colonies were stained with crystal violet (0.1 % in 20 % methanol). Colony numbers were visually assessed and colonies containing > 50 normal-appearing cells were counted. The experiment was performed in triplicate.

2.5.2.7. Cell cycle assay. As described above, cells treated with vehicle and NS-IONPs were harvested after 48 h, then fixed for 1 h at 4 °C in 70 % ethanol. Next, the cells were stained with PI (BioSure, Grass Valley, CA) for 15 min in the dark. FACS analysis was conducted using a Becton-Dickinson FACS Calibur flow cytometer (BD Biosciences, Germany). All assays were performed in triplicate.

2.5.2.8. Apoptosis assay. Cells undergoing apoptosis or necrosis were detected using the Annexin V-FITC Apoptosis staining/detection kit (Abcam). As described above, A549 cells treated with increasing concentrations of NS-IONPs were analyzed after 48 h in a humidified incubator (5 % CO_2, 37 °C). The cells were washed twice with PBS and stained with 5 μL Annexin V-FITC and 5 μL PI diluted in 500 μL Annexin binding buffer. The samples were then incubated in the dark for 5 min. Finally, the samples were analyzed under a fluorescent microscope (EVOS M7000, Invitrogen, Thermo Fisher Scientific).

2.5.2.9. Quantitative RT-PCR. The Trizol reagent was used to extract total RNA from colorectal cancer cells treated with NS-IONPs for 48 h. The reaction was performed using an Applied Biosystems thermocycler using the specific primers summarized in Table S1. Amplifications were conducted using the following protocol: initial denaturation (95 °C for 3 min), followed by 30 cycles of denaturation (95 °C for 1 min), primer annealing (57 °C for 30 *sec*), and synthesis (72 °C for 1 min), and a final extension step (72 °C for 7 min). Melting curve analysis was conducted to verify that each reaction produced only a single product. Gene expression was normalized to that of β-actin (Ganji et al., 2013).

2.5.2.10. Statistical analysis. Experiments were conducted in triplicate and repeated at least three times. The data were presented as the mean ± standard deviation (SD) of three independent experiments. Significant differences between the treatments were evaluated based on the SD. Pair-wise comparisons were conducted using Student's t-tests.

3. Results and discussion

Cancer is the most common cause of death worldwide and therefore has a major impact on society. Chemotherapy or radiation therapy builds up resistance to drugs in cancer patients, leading to more complications (Sung et al., 2020). Therefore, developing novel cancer treatments derived from natural sources has recently garnered increasing attention. Particularly, several recent studies have focused on the green synthesis of NPs from plants (Bardania et al., 2020) and microorganisms (Akhtar et al., 2013). Plant-based NPs are reportedly more efficient and have a higher yield than those fabricated via microbial-based synthesis (Sundaram and Augustine, 2012), and therefore numerous plants have been employed for NP synthesis. Here, the medicinal plant *N. sativa* was used for this purpose. *N. sativa* seeds contain essential fatty acids and a large number of phytochemical constituents with significant medicinal value. Previous studies have synthesized nickel oxide (Boudiaf et al., 2021), gold (Manju et al., 2016), and silver NPs (Almatroudi et al., 2020) using extracts from this plant. In this study, IONPs were synthesized from *N. sativa* seed hexane extract without the use of toxic or harmful chemicals.

Size is one of the main factors that limit the biomedical application of NPs. NPs with a diameter of >8 nm are retained in the kidney, which is referred to as the glomerular filtration barrier, leading to chronic renal failure. In contrast, NPs with a diameter smaller than 10 nm can easily pass through the renal system, thus preventing the retention of the drugs embedded on the NPs (Bujie et al., 2021). The NS-IONPs synthesized from *N. sativa* seed extract in this study had a diameter of 5–6 nm, whereas those produced from *Tridax procumbens* leaf extract had a diameter of 80–100 nm (Senthil and C., 2012). Therefore, this work offers a new strategy for the synthesis of highly retainable, biocompatible NPs that can clear the renal system. The extract also protected the NPs from oxidization without affecting their magnetic properties. Most importantly, the phytoconstituents or metabolites of the extracts present on the surface of the NS-IONPs played a therapeutic role against pathogenic bacteria and cancer cell lines.

3.1. Characterization of the NS-IONPs

The crystal structure and phase composition of the as-synthesized NS-IONPs were determined using XRD analysis. The NS-IONPs exhibited obvious peaks at 2θ angles of 30.10°, 35.59°, 43.15°, 53.63°, 56.95°, and 62.61°, corresponding to the (220), (311), (400), (422), (511), and (440) crystal planes of Fe_3O_4, respectively (Fig. 1a). This result was in accordance with previously reported data (JCPDS 79–0419) (Huang et al., 2019; Meng et al., 2021; Tang et al., 2021). The relatively high peak intensities indicate that the products were highly crystalline. The average crystallite size (D) was quantitatively calculated from the (311) peak using the Debye-Scherrer formula (Eq. (1)) (Wang et al., 2016):

$$D = (0.94\lambda/\beta d \cos\theta) \tag{1}$$

where λ represents the wavelength of the Cu Kα line, β_d denotes the full width at half maximum (FWHM) of the most intense diffraction peak of the (311) crystallographic plane. The average particle size calculated using Scherrer's equation was 6.46 nm, which was confirmed through FE-TEM analysis.

FTIR analysis was conducted to characterize and identify the functional groups bound specifically to *N. sativa* and the synthesized NS-IONPs (Rajan et al., 2020). The IR spectrum of *N. sativa* exhibited strong adsorption bands at 881, 1089, 1468, and 1743 cm^{-1} corresponding to the —HC═CH—, C—O, —C—H, and —C═O groups, while there were also two strong stretching vibration bands at 2932 and 2854 cm^{-1}, which can be attributed to the —C—H stretching vibrations of the $—CH_3$ and $—CH_2$ groups present in the polyphenols (thymoquinone, thymol, and carvacrol) of *N. sativa* (Mohammed et al., 2016 (2016).; Tara et al., 2020). The IR spectrum of the NS-IONPs exhibited adsorption bands at 3430 and 581 cm^{-1} corresponding to the stretching vibration modes of hydroxyl (—OH) groups and Fe—O bonds, respectively (Negut et al., 2018; Siddiqui et al., 2019). Additionally, the IR spectrum of Fe_3O_4 reflected the presence of $—CH_3$ and $—CH_2$ groups at 2932 and 2854 cm^{-1}, which indicates the involvement of the polyphenolic groups of *N. sativa* in the synthesis of the NS-IONPs (Fig. 1b). Similarly, Mahmoudi and his coworkers reported the encapsulation of the plant extract (hydro-alcoholic extract of *Physalis alkekengi*-L) on to surface of NPs improving its stability and biological activity (antioxidant properties) (Mahmoudi et al., 2019).

The formation and stability of the NS-IONPs produced via the addition of *N. sativa* plant extract to a ferric chloride ($FeCl_3$) precursor were investigated using UV–vis spectral analysis. Fig. 1c shows that $FeCl_3$ and *N. sativa* exhibited strong adsorption bands at 317 and 257 nm, respectively (Yew et al., 2016; Saif et al., 2019). Upon adding the *N. sativa* extract to the $FeCl_3$ solution in the presence of citric acid as the initial nucleating agent for the formation of Fe NPs, the light-brown solution rapidly turned dark black, which is indicative of NS-IONP formation (Fig. S1). UV–vis analysis of NS-IONP revealed continuous absorption between 200 and 600 nm, which was consistent with the characteristics of commercial Fe_3O_4 NPs and confirmed the high dispersibility and stability of the as-synthesized NS-IONPs (Geinguenaud et al., 2015). During the formation of the NS-IONPs, the phytoconstituents of *N. sativa* acted as capping agents following the initial nucleation of Fe NPs by citric acid.

The zeta potential is a measure of the electrostatic potential of the surface of NPs, which is often used to measure the stability of the colloidal suspension. The zeta potential of IONPs is −24.35 mV (Fig. S2) while the zeta potential of NS-IONPs synthesized using *N. sativa* extract was −15.61 mV. The potential decrease is mainly due to the positively charged polyphenols which are incorporated in the particles. The strong negativity indicating that the NS-IONP suspension was highly active and that the NPs were not agglomerated (Fig. S2a) (Kędzierska et al., 2021). More importantly, the phytoconstituents of *N. sativa* contain large numbers of –OH groups that act as capping agents for the NS-IONPs and generate a repulsive force that leads to the formation of a highly stable NP suspension without agglomeration (Kajani and A.-k., 2019). Moreover, the polyphenolic side chains (methoxy group) of the phytoconstituents of *N. sativa* enhance the activity of the NPs (Shin et al., 2018). These stable NS-IONPs are highly suitable for use in antibacterial and anticancer analyses.

The oxidation state and surface elemental composition of the as-synthesized NS-IONPs were analyzed using XPS and the results are presented in Fig. 2. The wide-scan spectrum of Fe_3O_4 (Fig. 2a) reveals the presence of iron (Fe), carbon (C), and oxygen (O) (Tang et al., 2021; Madhuvilakku et al., 2017; Reddy et al., 2018), whereas the deconvoluted C 1s spectrum of the NS-IONPs (Fig. 2b) exhibited an intense peak at 284.90 corresponding to sp^2 C—C bonds, with the peaks at 286.44 and 288.71 being ascribed to the presence of C—O and –COOH, respectively (Madhuvilakku et al., 2017). The O 1s spectrum of the NS-IONPs was deconvoluted into three peaks at 530.00, 531.31, and 533.13 eV, which may be attributed to the presence of lattice oxygen in metal oxides (Fe—O),

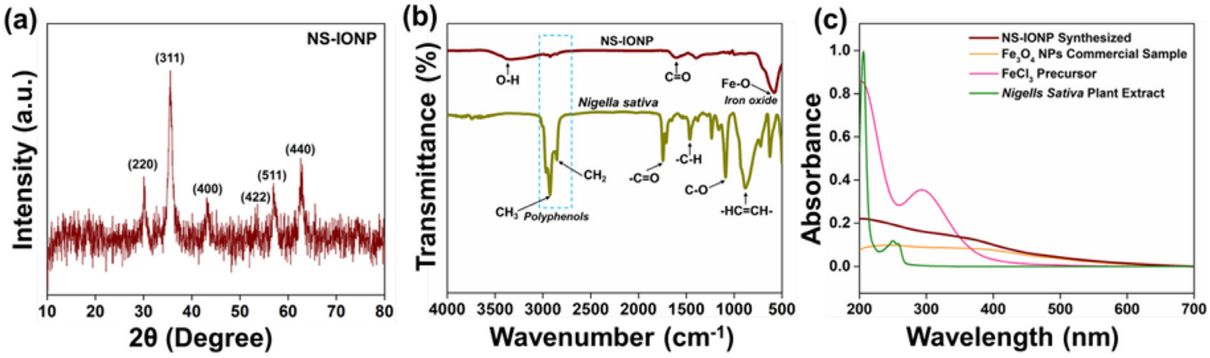

Fig. 1 (a) X-ray diffraction analysis of the NS-IONPs, (b) Fourier transformation infrared spectra of *N. sativa* and the IONPs, and (c) UV–vis analysis of the NS-IONPs, *N. sativa*, $FeCl_3$, and commercial Fe_3O_4.

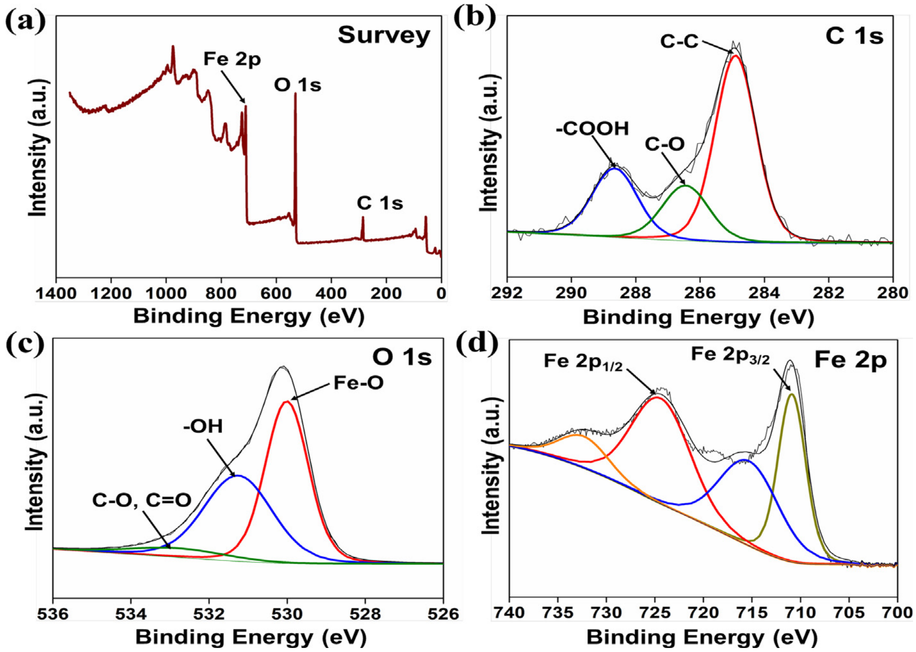

Fig. 2 X-ray photoelectron spectra of the NS-IONPs. (a) Survey, (b) C 1s, (c) O 1s, and (d) Fe 2p spectra.

residual oxygen-containing groups (O—H), and surface oxygen complexes of the carbon phase (C—O and C=O), respectively (Fig. 2c) (Tang et al., 2021; Rajan et al., 2020; Reddy et al., 2018). The high-resolution XPS spectrum of Fe 2p (Fig. 2d) exhibited two central $Fe2p_{3/2}$ and $Fe2p_{1/2}$ spin–orbit doublets at 710.93 and 724.80 eV, as well as corresponding satellite peaks at 715.91 and 733.06 eV, respectively, which may be attributed to the presence of Fe^{3+} and Fe^{2+} ions. The energy difference (ΔE) between $Fe2p_{3/2}$ and $Fe2p_{1/2}$ was 13.7 eV, which is in good agreement with the standard Fe_3O_4 XPS spectrum (Madhuvilakku et al., 2017).

HR-SEM images were used to investigate the surface morphology of the NS-IONPs (Fig.. S3). NS-IONPs with a rough surface and a spherical morphology were observed, and the diameter of these NPs was < 50 nm. The particles at the surface were agglomerated, which may be due to the magnetic nature of the Fe_3O_4 NPs (Yew et al., 2016; Rahman et al., 2017). The chemical composition of the NS-IONPs analyzed using SEM-EDX confirmed the presence of iron and oxygen, with atomic percentages of 45.01 % and 54.22 %, respectively (Fig. S3).

The morphology, size, and crystallinity of the as-synthesized NS-IONPs were characterized via HR-TEM analysis (Fig. 3). The majority of the NS-IONPs were roughly spherical and exhibited a narrow size distribution ranging from 5 to 10 nm. The smaller size of the NS-IONPs indicated that *N. sativa* acted as a capping agent, thus inhibiting the growth of NPs. Similarly, in another interesting study, when glycine was introduced during the synthesis of the nanoparticles, the reaction mixture produced magnetite nanoparticles with diameters of 5.35 ± 1.13 nm and when it was not, 8.74 ± 1.18 nm NPs were synthesized (Bardania et al., 2013; Bardania and Raheb, 2019). TEM image analysis demonstrated that some of the NS-IONPs formed agglomerations, which may be due to the magnetic nature of smaller-sized NPs (Fig. 3 a, b) (Shin et al., 2018). The particle size distribution of 56 particles was measured using the ImageJ software (Fig. 3c, inset) and the mean particle size was 6.10 ± 0.89 nm (SD = 0.89 nm), which was consistent with the average particle size calculated using XRD analysis (6.60 nm) (Fig. 1a). The NPs also showed an inter-planar separation (i.e., lattice fringe width; Fig. 3d) of 2.3 Å, which confirmed the successful synthesis of NS-IONPs (Fig. 3d) (Siddiqui et al., 2019). The selected area electron diffraction (SAED) pattern of the NS-IONPs showed six white spotty diffraction rings corresponding to the (220), (311), (400), (422), (440), and (511) planes of spinel magnetite, illustrating the polycrystalline nature of the NPs and agreeing with the XRD results (Fig. 3e) (Dutta et al., 2017). EDS elemental mapping revealed the presence of Fe, C, and O, with Fe and O concentrated in the central region of the NS-IONPs. TEM-EDS analysis showed that the as-synthesized NS-IONPs were composed of Fe (14.05 %), O (26.78 %), and C (59.17 %) (Fig. 3f) (Kajani and A.-k., 2019) (Fig. S4).

3.2. Biological activities

3.2.1. Antibacterial activity analysis

The antibacterial activity of the synthesized IONPs and NS-IONPs at 60 °C was analyzed against three medically important pathogenic microorganisms: *Staphylococcus aureus, Escherichia coli*, and *S. typhimurium*. IONPs did not show any effect on the microorganisms. Similar report was recently published which showed that magnetic nanoparticles did not exhibit toxic effect on both bacterial as well as eukaryotic cells (Bardania and Raheb, 2019). Recently the metal–polyphenol complexes has gained attention due to its versatile biochemical functions (catalysis and anti-oxidation process) as biocompatible ligands (Kim et al., 2021). The NS-IONPs exhibited antibacterial activity against the gram-negative bacteria *E. coli* and *S. typhimurium* but had little effect on the gram-positive bacterium *Staphylococcus aureus*. *E. coli* is a non-

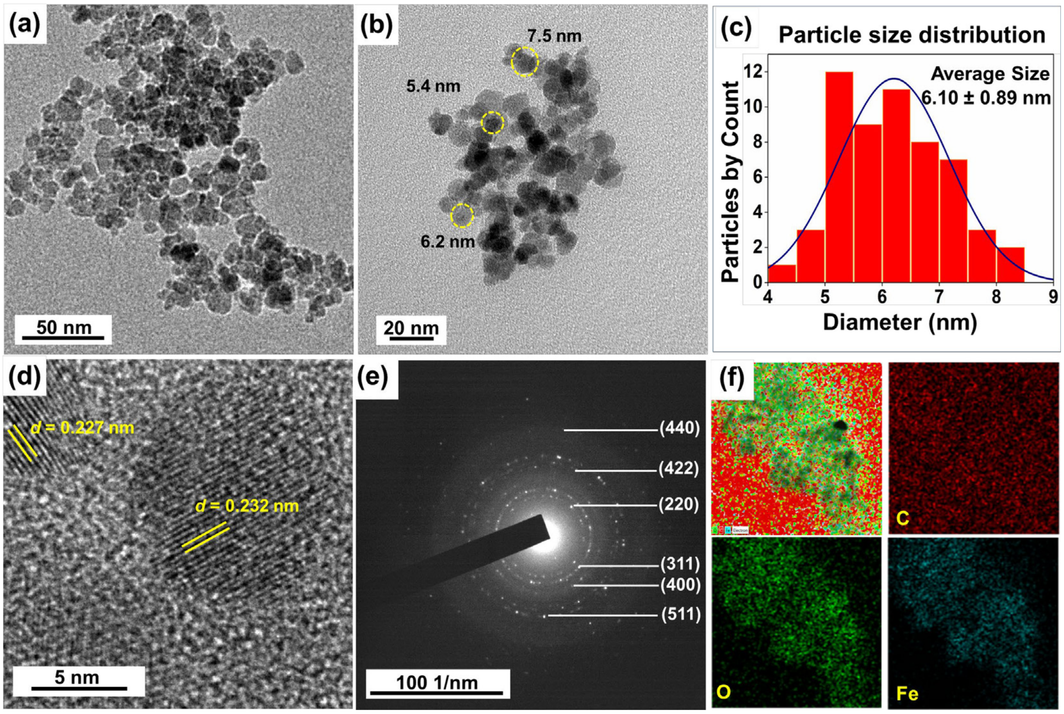

Fig. 3 High-resolution transmission electron microscopy (HR-TEM) images of (a,b) NS-IONPs at different magnifications, (c) particle size distribution of selected NS-IONPs, (d) lattice fringe width of the NS-IONPs, (e) SAED pattern of the NS-IONPs, and (f) elemental mapping of the NS-IONPs showing the presence of Fe, O, and C.

spore-forming commensal species that harmoniously coexists in the human intestine as part of the microbiota, helping to prevent the colonization of harmful pathogenic bacteria. However, some strains cause food poisoning, pneumonia, and urinary tract infections (Delmas et al., 2015). *Salmonella typhimurium*, a facultative anaerobic pathogenic bacterium causes typhoid fever, a high fever with neurological abnormalities (Chaudhuri et al., 2018). As summarized in Table 1, the NS-IONPs had a dose-dependent effect on both of the aforementioned gram-negative pathogenic bacteria. A concentration of 100 µg/mL of NS-IONPs produced strong antibacterial activity (19.3 mm) against *E. coli*, similar to the effect exhibited by 10 µg/mL of tetracycline, a commercial antibiotic (Fig. 4). Furthermore, the diameter of the zone of inhibition against *S. typhimurium* NS-IONPs exhibited a minimum size of 12.4 mm and maximum of 14.2 mm at a NS-IONP concentration of 25 µg/mL and 100 µg/mL, respectively. Similar research has been conducted using silver NPs synthesized using *N. arvesis* seed extract. An analysis of the antibacterial effect of the silver NPs on six bacterial species (*Bacillus subtilis, Streptococcus pyogenes, E. coli, S. typhi, S. aureus,* and *Proteus mirabilis*) demonstrated that silver NPs dose-dependently inhibited the growth of the pathogenic bacteria (Chahardoli et al., 2017).

Our bacterial growth inhibitory assays also confirmed the inhibitory effect of NS-IONPs on the growth of gram-negative bacteria but only negligible effects on the gram-positive bacterium *S. aureus* (Fig. S5). The higher concentration (>400 µg/mL) of NPs exhibited significant effect on *S. aureus*. The NS-IONPs can easily penetrate the cell membrane of gram-negative bacteria compared to the gram-positive bacteria. The positively charged methoxy protons of the polyphenols would have positively affected the activity. Polyphenols have already been reported to exhibit significant antibacterial activity. The observations suggested that interaction likely between the positively charged polyphenols with the negatively charged bacterial cell surface. SEM imaging illustrated the potential effect of NS-IONPs on *E. coli*. The treated bacterial

Table 1 Antibacterial activity of the NS-IONPs.

Bacterial species	Control (Tetracycline)	NS-IONPs		
	10 µg/mL	25 µg/mL	50 µg/mL	100 µg/mL
E. coli	18.6 ± 0.12	11.2 ± 0.15	15.8 ± 0.14	19.3 ± 0.04
Salmonella typhi	17.4 ± 0.06	12.4 ± 0.26	13.3 ± 0.12	14.2 ± 0.11

The numbers represent the zone of inhibition in mm.
Each value represents mean value ± standard deviation of three replicates.

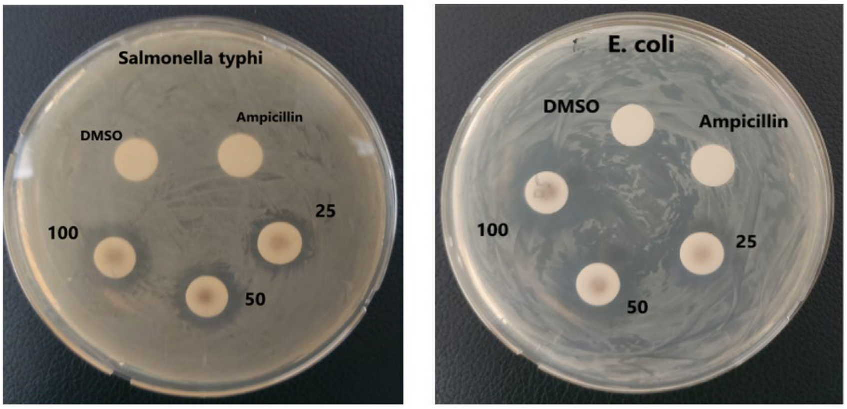

Fig. 4 Antibacterial activity of NS-IONPs.

samples appeared smaller (i.e., an indication of growth retardation) compared to the control and the surface morphology was strongly affected, with many damaged bacteria being detected (Fig. 5). These findings contradicted those of a previous study conducted by another research group. Specifically, the authors studied the effect of iron and gold nanoparticles on *E. coli* and found that these particles abruptly increased the size of *E. coli* (Shin et al., 2018). *S. typhimurium* was comparatively less affected (only its surface morphology was modified) than *E. coli* (Fig. S6).

3.2.2. *Anticancer activity analysis*

3.2.2.1. CCK-8 assay. The cytotoxic effect of IONPs and NS-IONPs was examined using CCK-8 assays with colorectal cancer (HCT116) and lung cancer (A549) cell lines at 24- and 48-h intervals. The IONPs did not exhibit any effect on both the cancer cell lines. The results were presented as IC_{50} calculated in µg/mL (Table 2). The toxicity of the NS-IONPs was examined at different concentrations (1.56 to 100 µg/mL) and compared with that of the control. Higher NS-IONP concentrations had stronger inhibitory effects on cell growth (Fig. 6 a and b; Table 2) and these effects were also time-dependent. The cells were initially subjected to treatment for 24 h, but there was no significant effect compared to the control. Therefore, the treatment time was increased to 48 h, after which a significant toxicity effect was apparent. First, NS-IONPs were used to treat HCT116 cells, and the proliferation assay results revealed that the NPs had a significantly more potent cytotoxic activity ($IC_{50} = 89.5$ µg/mL; $p < 0.001$) (Fig. 6a) in a dose- and time-dependent manner. Fig. 6b presents the CCK-8 assay results, which confirm the significant *in vitro* cytotoxic effect of the NS-IONPs against A549 cancer cells ($p < 0.001$). High concentrations of NS-IONPs showed promising cytotoxic activity against the tested cell lines. In a

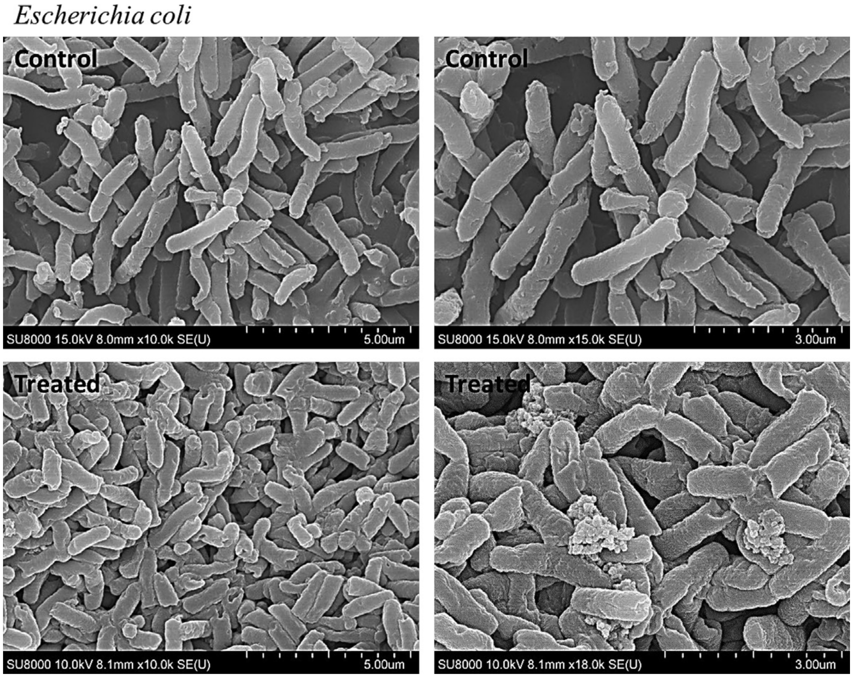

Fig. 5 Scanning electron microscopy images of *E. coli* - control (before treatment) and treated (after treatment with NS-IONPs).

Table 2 Effect of different concentrations of NS-IONPs on two cancer cell lines.

Concentration (μg/ml)	**% Cell viability (% Inhibition)**							
	1.56	**3.125**	**6.25**	**12.5**	**25**	**50**	**100**	**IC_{50}**
HCT-116	86.27 (13.73)	82.52 (17.48)	76.94 (23.06)	64.53 (35.47)	60.00 (40.00)	55.92 (44.08)	52.81 (47.19)	**89.50**
A549	95.75 (4.25)	88.64 (11.36)	84.32 (15.68)	67.31 (32.69)	28.87 (71.13)	13.22 (86.78)	4.03 (95.97)	**18.75**

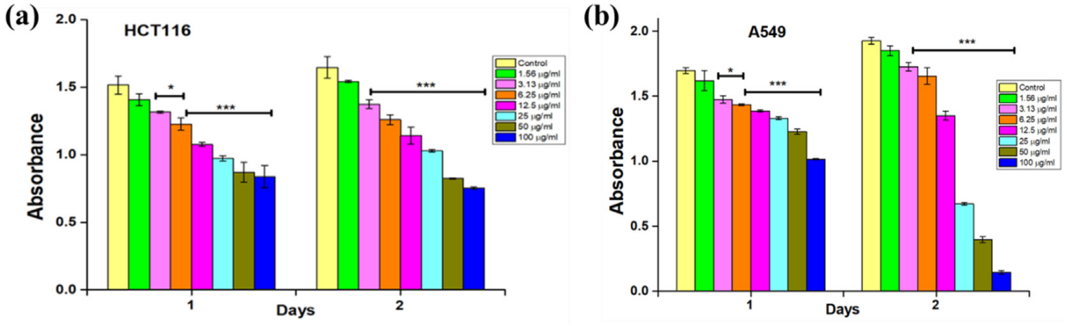

Fig. 6 *In vitro* cytotoxicity against (a) HCT-116 cells and (b) A549 cells assessed using CCK-8 assays. The values represent the mean ± SD (n = 3). Statistical significance: *** $P < 0.001$ and * $P < 0.05$.

previous study, the IC_{50} of an *n*-hexane extract of *N. sativa* seeds against A549 cell lines was reported to be 31.00 μg/mL (Bourgou et al., 2012), whereas the IC_{50} of the NS-IONPs in the present study was 18.75 μg/mL. These results demonstrate the superior effects of NS-IONPs compared to the free extract. Magnetic IONPs synthesized from an aqueous extract of the seaweed *Sargassum muticum* have also been reported to exert similar cytotoxic effects. Specifically, the IC_{50} values of the aforementioned IONPs in the HeLa and HepG2 cell lines were 12.5 μg/mL and 23.83 μg/mL, respectively (Namvar et al., 2014). Table 2 summarizes the percentages of cell viability and inhibition at 48 h post-treatment. At a higher concentration of 100 μg/mL, the A549 cells exhibited maximum inhibition of 95 % compared to 47.15 % in the HCT116 cell line. Thus, the NS-IONPs at higher concentrations exhibited a more promising cytotoxic effect against A549 cancer cells compared to the HCT116 cells.

3.2.2.2. Cytomorphological changes. Significant cytomorphological changes were observed in cancer cell lines, with the cell density decreasing as the concentration of the NS-IONPs increased. Fig. S7 clearly shows nucleus shrinkage in all the cancer cell lines, with the A549 cells exhibiting the highest degree of nucleus shrinkage. The yellow arrows in Fig. S7 show cells undergoing cell lysis. The results clearly demonstrate that NS-IONPs exhibit more potent cytotoxic activity against A549 cells compared to the HCT116 cell lines. Fig. S8a presents the accumulation of NPs inside A549 cells, with lysis occurring after 48 h of treatment. The NS-IONPs were absorbed into all cell types, as demonstrated by the absence of NPs in the growth media (Fig. S8b). Similarly, Almatroudi et al. (Almatroudi et al., 2020) analyzed silver NPs synthesized from *N. sativa* seed extract and reported morphological changes in breast cancer cell lines, highlighting their potential for use in biomedical applications. Cytotoxicity induced by different NPs has been ascribed to a variety of mechanisms.

3.2.2.3. SEM and TEM analysis of the cells. In the present study, SEM imaging confirmed that the cancer cells shrank upon treatment with NS-IONPs compared to the control (Fig. 7). The EDX results for the control A549 cell lines before and after NS-IONPs treatment are illustrated in Fig. S9. The NS-IONPs tended to bind to the membrane, as the EDX analysis clearly shows the loss of phosphorus, which is one of the principal components of the plasma membrane. Similar effects were also observed on *E. coli* (Fig. S10). Specifically, the NS-IONPs were bound to the surface of the cells. The TEM images (Fig. 7c and d) demonstrated that the bound NS-IONPs were progressively absorbed into the cell through the membrane and formed aggregates both inside and outside of the cells. After 48 h of treatment, cell lysis was also observed. Overall, our results demonstrated that NS-IONPs exhibited more significant anticancer activity against A549 cancer cells than against HCT116. Youhannayee et al.(Youhannayee et al., 2019) reported that the uptake of coated NPs was significantly higher in prostate cancer cells compared to normal benign cells. The examined TEM images demonstrated no specific interaction of NP with the cell organelles. However, each cell type exhibited unique NP uptake mechanisms (Youhannayee et al., 2019). In the present study, the particles were readily absorbed into the cells and accumulated in the

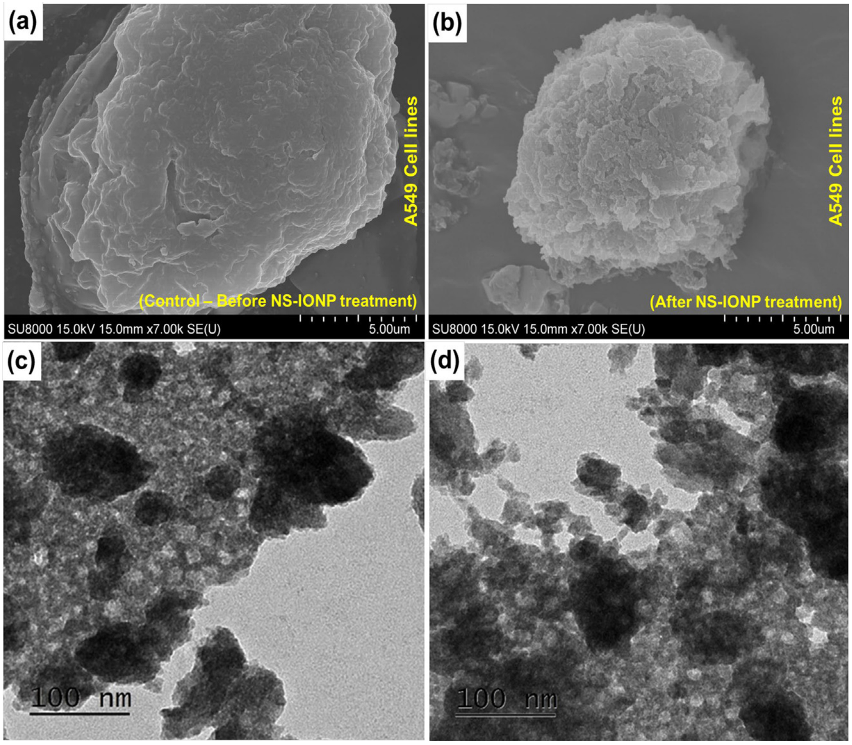

Fig. 7 Scanning electron microscope images of the A549 cells – (a) Control – before treatment, (b) cells after treatment with NS-IONPs; transmission electron microscope images of the A549 cell lines (c) cell uptake of NS-IONPs, some particles were slightly aggregated as they were absorbed into the cell, (d) cells undergoing lysis after 48 h of NS-IONP treatment.

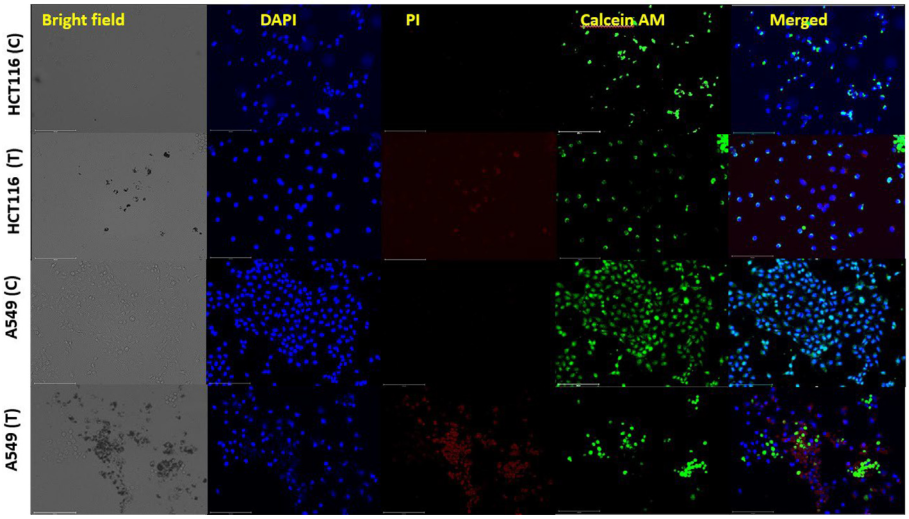

Fig. 8 Cellular viability assay illustrating the live/dead cells due to the effect of NS-IONPs on HCT116 and A549. C, control; T, treated.

cytoplasm, resulting in cell lysis. In the future, this could be used as a template to study the molecular mechanisms underlying the anticancer activity of NPs (Fig. 7c and d).

3.2.2.4. Viability assay. A cellular viability assay was performed using the live cell stain Calcein-AM and the dead cell stain propidium iodide (PI). Fig. 8 illustrates the control (untreated) and NS-IONP-treated (50 μg/ml) HCT116 and A549 cell lines at 48 h post-treatment. As expected, the control samples were not stained with PI, and therefore all of the live cells were stained green. DAPI was used to stain the nuclei, which facilitates the estimation of the number of cells in the view window. DAPI staining also demonstrated that the NS-IONP treatment substantially decreased the live cell counts in both the cell lines. Mortality was observed in both NP-treated cell lines, with the A549 cell line exhibiting a higher percentage of dead cells. The control and NP-treated A549 cells exhibited significant differences in mortality rates, as demonstrated by

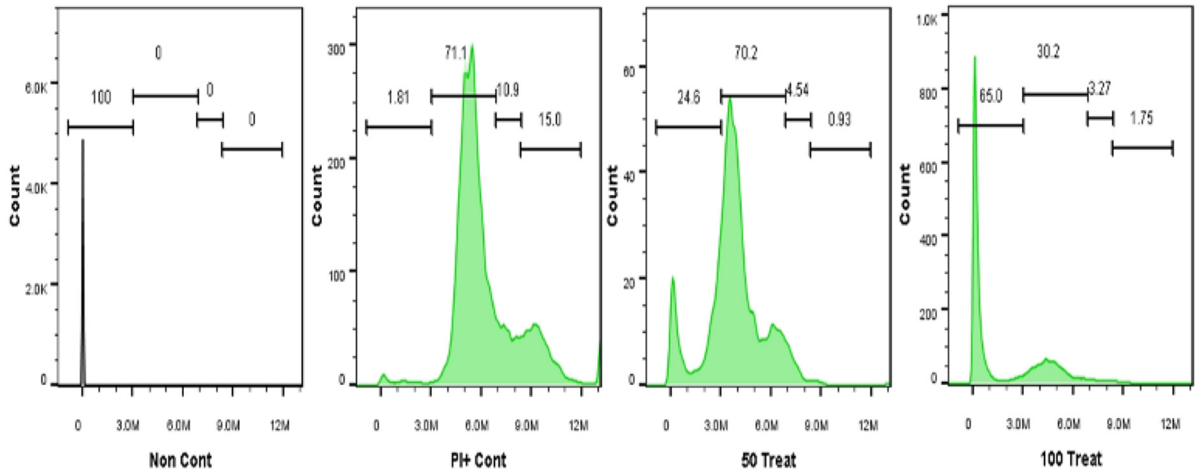

Fig. 9 Cell cycle effects of NS-IONPs in lung cancer cells (A549). "50 Treat" and "100 Treat" represent cells treated with NS-IONPs at concentration of 50 µg/ml and 100 µg/ml, respectively.

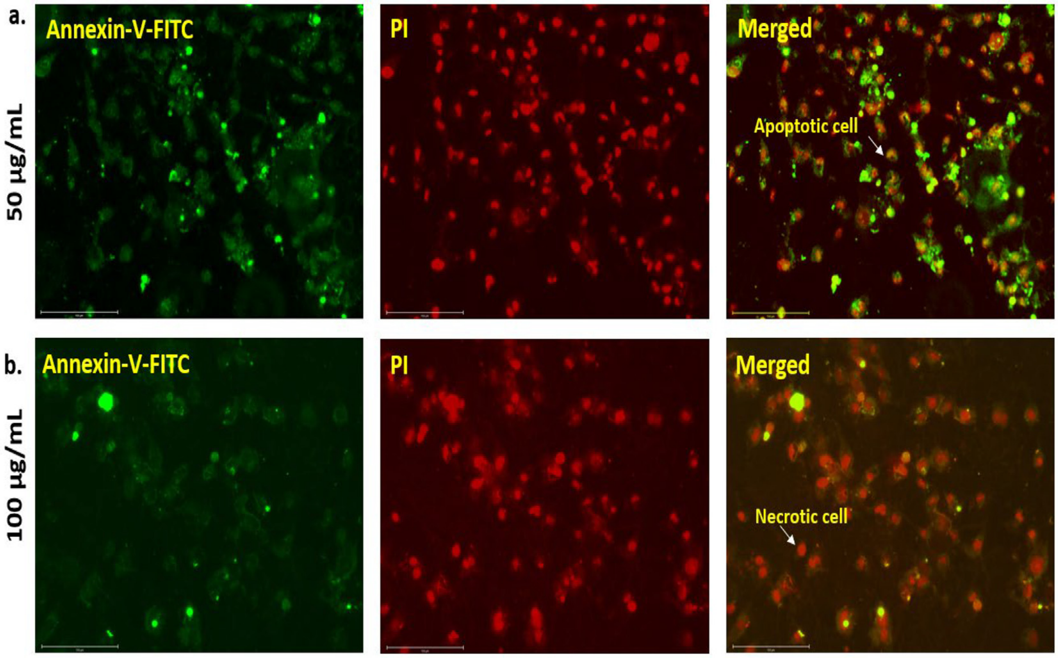

Fig. 10 A549 cells induced with (a) 50 µg/ml and (b) 100 µg/ml of NS-IONPs for 48 h and stained with the Annexin V-FITC Apoptosis detection kit. The cells in apoptotic/necrotic state were detected.

Calcein-AM staining. Concretely, the merged image of the treated A549 cells demonstrated that the NS-IONPs had detrimental effects. Fig. 8 also clearly shows that the HCT116 cells were substantially less affected by the NS-IONPs.

3.2.2.5. Clonogenicity assay. The ability of a single cell to proliferate indefinitely to form a colony was analyzed through a clonogenic assay or colony formation assay. Here, these clonogenic assays were conducted to assess the cytotoxicity of the NS-IONPs (i.e., the effects of NPs on cell proliferation). After treatment in an NP environment, a cell is deemed to be viable if it survives and can divide to form clones (a small colony of genetically identical cells). Fig. S11 shows the results of the clonogenic assay. In cell line A549, the formation of the colony was significantly inhibited in the NS-IONP-containing medium (100 µg/ml) compared to untreated cells, suggesting that their effects were additive. As expected, the sensitivity of the HCT-116 cell line was significantly lower than that of the A549 cells. Therefore, our findings demonstrated that the NS-IONPs initiate an irreversible cell arrest process or otherwise exert 'cidal' and not 'static' activity.

3.2.2.6. Cell cycle analysis. Cell proliferation and cell survival are often related to cell cycle molecules (Maddika et al., 2007). According to previous studies, cancer cells with faulty checkpoints are more susceptible to anti-cancer drugs

(Gabrielli et al., 2012). Thus, compounds that interfere with the cell cycle checkpoints can be effective anticancer agents. Here, cell cycle analyses were conducted by staining the DNA of the A549 cells with PI (DNA binding dye with an absorption maximum of 535 nm) and their fluorescence was analyzed using flow cytometry. First, the DNA content in treated and untreated A549 cells was analyzed. The DNA content was characterized by measuring the fluorescence emission by the PI-DNA complex, which has a maximum absorption at 617 nm. Our findings indicated that the NS-IONPs induced G0/G1 arrest in the A549 cells (Fig. S11 b & c), thereby inducing apoptosis or necrosis. Furthermore, there was a decrease in the percentage of cells in the control group (69.81 %) (Fig. S11 a) compared to the high concentration treatment (49.56 %) at the G0/G1 phase. In contrast, we observed an increase in the number of cells in the sub-G0 peak, which may be attributed to irreversible DNA damage. The percentage of dead cells increased considerably in the 100 µg/ml treatment (65 %) compared to the control (0.53 %). As illustrated in Fig. 9, NS-IONPs dose-dependently decreased the percentage of cells in the S phase. Specifically, the percentage of control cells in the S phase was nearly 10.9 %–4.08 % but decreased to 4.54 %–7.96 % and 3.27 %–7.49 % at 50 µg/ml and 100 µg/ml NS-IONPs, respectively. Therefore, the cells arrested at the G0/G1 stage due to accumulation of NS-IONPs underwent late apoptosis or necrosis. Silver nanoparticles at 25 and 80 µg/mL have also been found to induce G2/M arrest. Furthermore, in another study that evaluated the cytotoxicity of superparamagnetic iron oxide nanoparticles (SPION), significant apoptosis was observed at a concentration of 80×10^{-3} M (Mahmoudi et al., 2009). The cells were arrested within 48 h of treatment in the G0/G1 phase, indicating that NS-IONPs can arrest the cell cycle. These cells will eventually undergo apoptosis (a desirable form of cell death in cancer) if they are arrested at a specific stage of the cell cycle. DNA damage is the primary factor leading to necrosis and cell death, as depicted in Fig. 9.

3.2.2.7. *Apoptosis assay*. Apoptosis (programmed cell death) leading to necrosis has been proven to have a major impact on tumor regression. This process is spontaneous and occurs due to external stimuli such as the administration of drugs or anticancer agents. Unlike flow cytometry, which cannot distinguish between apoptotic and necrotic cells, the annexin V-FITC apoptosis detection method is a very sensitive approach developed to identify the different cells undergoing apoptosis and necrosis (Baskić et al., 2006). Here, we observed that the cells that absorbed high concentrations of NS-IONPs spontaneously underwent necrosis. A549 cells were exposed to 50 and 100 µg/ml of NS-IONPs and were incubated for 48 h, then stained with the Annexin V-FITC apoptosis detection kit to detect the cells in apoptotic/necrotic state. As illustrated in Fig. 10, a large percentage of the cells underwent necrosis at high concentrations of NS-IONPs. Apoptotic and necrotic cells are easily distinguished from normal healthy cells. Shrinking and rounding of the cells was also observed. The early apoptotic cells exhibited a shrunk and condensed nucleus with chromatin, which was manifested as bright green arcs. Late apoptotic cells and necrotic cells appeared as condensed shrunk red nuclei.

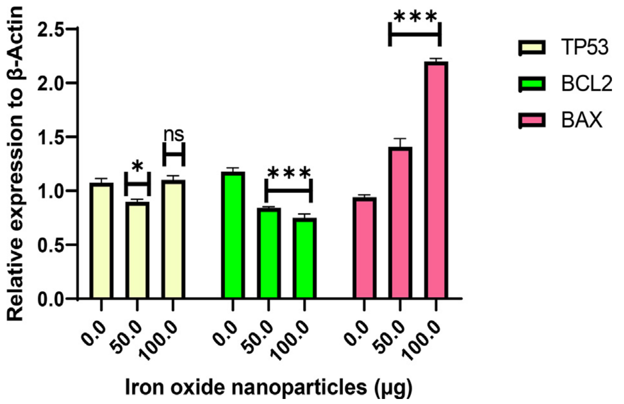

Fig. 11 Effects of different NS-IONP concentrations (µg/mL) on the expression of signal molecules involved in the control of apoptosis. Each value represents the mean ± standard deviation, *$p < 0.05$; *** $p < 0.001$, ns-not significant.

3.2.2.8. *Quantitative RT-PCR*. Additionally, quantitative RT-PCR (qRT-PCR) analysis was performed to verify the expression of apoptosis-related genes at the messenger RNA level (Fig. 11). The induction of apoptosis is generally considered to be an effective strategy for cancer treatment. Biogenic NPs induced programmed cell death in cancer cells through activation of apoptotic genes (Datkhile et al., 2021). Thus, the expression of BCL2 (an anti-apoptotic gene) and BAX (a pro-apoptotic gene) was examined before and after treatment with different (50 and 100 µg/mL) concentrations of NS-IONPs. Several studies have reported that increased BAX expression and decreased BCL2 expression induces cell death (Nachmias et al., 2004). Cells were treated for 48 h with either a vehicle (control) or NS-IONPs and mRNA was extracted to conduct qRT-PCR analyses using β-actin as a reference gene. NS-IONP treatment significantly ($p < 0.001$) increased BAX mRNA expression levels and decreases BCL2 levels but treatment at 100 µg/mL did not significantly affect the expression levels of P53 in the A549 cell lines compared to the control. But at low concentration of 50 µg/mL there was significant ($p < 0.05$) expression. Collectively, these findings indicate that NS-IONPs inhibit cell proliferation by inducing cell death, suggesting that these NPs could be used as a basis for the development of novel cancer treatments.

4. Conclusion

To the best of our knowledge, our study is the first to characterize the cytotoxic activity of IONPs synthesized using a hexane extract from *N. sativa* seeds. The green synthesis of NS-IONPs (size 5–6 nm) using *N. sativa* hexane extract was validated by UV–vis, XRD, FTIR, XPS, SEM, EDX, HR-TEM, and EDS analysis. The NS-IONPs were conjugated with polyphenols of the *N. sativa* extract. Along with citric acid, these polyphenols acted as reducing and capping agents, thus enabling the synthesis of NPs with lower aggregation and higher reactivity. Moreover, the NS-IONPs exhibited bactericidal effects against gram-negative bacteria. NS-IONPs dose- and time-dependently exerted cytotoxic effects on the A549 and HCT116 cell lines, with the former being the most sensitive. The cells were arrested at G0/G1 phase extended their G0 phase to undergo necrosis due to accumulation of NS-IONPs. Collectively, our findings demonstrated that NS-IONPs are highly efficient anticancer and antibacterial agents. The NS-IONPs demonstrated efficient cellular uptake, which would enhance their therapeutic efficacy and make them suitable candidates for biomedical applications. Future studies should focus on elucidating the molecular mechanisms responsible for the inhibition of cancer cell proliferation by NS-IONPs.

CRediT authorship contribution statement

Sheik Aliya: Conceptualization, Methodology, Investigation, Writing – original draft. **Muruganantham Rethinasabapathy:** Investigation, Writing – review & editing. **Jingon Yoo:** Writing – review & editing. **Eunsu Kim:** Writing – review & editing. **Joo-Yoon Chung:** Writing – review & editing. **Jong-Ho Cha:** Conceptualization, Supervision, Writing – review & editing. **Yun Suk Huh:** Conceptualization, Supervision, Writing – review & editing.

Declaration of Competing Interest

The authors declare that they have no known competing financial interests or personal relationships that could have appeared to influence the work reported in this paper.

Acknowledgment

This work was supported by the South Korean Ministry of Science, ICT & Future Planning through the National Research Foundation (2021R1A5A6002853, 2020R1C1C1005631, and 2022R1I1A1A01072069).

Appendix A. Supplementary material

Supplementary data to this article can be found online at https://doi.org/10.1016/j.arabjc.2023.104703.

References

Aisida, S.O., Madubuonu, N., Alnasir, M.H., Ahmad, I., Botha, S., Maaza, M., Ezema, F.I., 2020. Biogenic synthesis of iron oxide nanorods using Moringa oleifera leaf extract for antibacterial applications. Appl. Nanosci. 10, 305–315.

Akhtar, M.S., Panwar, J., Yun, Y.-S., 2013. Biogenic synthesis of metallic nanoparticles by plant extracts. ACS Sust. Chem. Eng. 1, 591–602.

Alam, T., Khan, R.A.A., Ali, A., Sher, H., Ullah, Z., Ali, M., 2019. Biogenic synthesis of iron oxide nanoparticles via Skimmia laureola and their antibacterial efficacy against bacterial wilt pathogen *Ralstonia solanacearum*. Mater. Sci. Eng. C 98, 101–108.

Almatroudi, A., Khadri, H., Azam, M., Rahmani, A.H., Khaleefah, A., Khaleefah, F., Khateef, R., Ansari, M.A., Allemailem, K.S., 2020. Antibacterial, antibiofilm and anticancer activity of biologically synthesized silver nanoparticles using seed extract of *Nigella sativa*. Processes 8, 388.

Augustine, R., Hasan, A., 2020. Multimodal applications of phytonanoparticles. In: Thajuddin, N., Mathew, S. (Eds.), Phytonanotechnology, Elsevier, pp. 195-219.

Ayyanaar, J.S., Kesavan, M.P., Balachandran, C., Rasala, S., Rameshkumar, P., Aoki, S., Rajesh, J., Webster, T.J., Rajagopal, G., 2020. Iron oxide nanoparticle core-shell magnetic microspheres: Applications toward targeted drug delivery. Nanomed. Nanotechnol. Biol. Med. 24, 102134–102145.

Bardania, H., Raheb, J., Mohammad-Beigi, H., Rasekh, B., Arpanaei, A., 2013. Desulfurization activity and reusability of magnetite nanoparticle–coated Rhodococcus erythropolis FMF and R. erythropolis IGTS8 bacterial cells. Biotechnol. Appl. Biochem. 60, 323–329.

Bardania, H., Raheb, J., Arpanaei, A., 2019. Investigation of desulfurization activity, reusability, and viability of magnetite coated bacterial cells. Iran. J. Biotechnol. 17, 14–20.

Bardania, H., Mahmoudi, R., Bagheri, H., Salehpour, Z., Fouani, M. H., Darabian, B., Khoramrooz, S.S., Mousavizadeh, A., Kowsari, M., Moosavifard, S.E., Christiansen, G., 2020. Facile preparation of a novel biogenic silver-loaded Nanofilm with intrinsic anti-bacterial and oxidant scavenging activities for wound healing. Sci. Rep. 10, 6129.

Baskić, D., Popović, S., Ristić, P., Arsenijević, N.N., 2006. Analysis of cycloheximide-induced apoptosis in human leukocytes: Fluorescence microscopy using annexin V/propidium iodide versus acridin orange/ethidium bromide. Cell Biol. Int. 30, 924.

Boudiaf, M., Messai, Y., Bentouhami, E., Schmutz, M., Blanck, C., Ruhlmann, L., Bezzi, H., Tairi, L., Mekki, D.E., 2021. Green synthesis of NiO nanoparticles using Nigella sativa extract and their enhanced electro-catalytic activity for the 4-nitrophenol degradation. J. Phys. Chem. Solids. 153, 110020.

Bourgou, S., Pichette, A., Marzouk, B., Legault, J., 2012. Antioxidant, anti-inflammatory, anticancer and antibacterial activities of extracts from *Nigella sativa* (black cumin) plant parts. J. Food Biochem. 36, 539–546.

Bujie, D., Jiang, X., Das, A., Zhou, Q., Mengxiao, Y., Jin, R., Zheng, J., 2021. Glomerular barrier behaves as an atomically precise bandpass filter in a sub-nanometre regime Nanomaterials and Neoplasms. Jenny Stanford Publishing, pp. 1133–1160.

Byun, M.J., Lim, J., Kim, S.N., Park, D.H., Kim, T.H., Park, W., Park, C.G., 2022. Advances in Nanoparticles for Effective Delivery of RNA. Therapeutics BioChip., J 16, 128–145.

Chahardoli, A., Karimi, N., Fattahi, A., 2017. Biosynthesis Characterization, antimicrobial and cytotoxic effects of silver nanoparticles using *Nigella arvensis* seed extract Iran. J. Pharm. Res. 16, 1167.

Chaudhuri, D., Roy Chowdhury, A., Biswas, B., Chakravortty, D., 2018. *Salmonella Typhimurium* infection leads to colonization of the mouse brain and is not completely cured with antibiotics. Front. Microbiol. 9.

Dariya, B., Govardhanagiri, S., Rajitha, B., Aliya, S., Alam, A. and Nagaraju, G.P., 2019. Curcumin and genistein enhance the sensitivity of pancreatic cancer to chemotherapy. In: G. P. Nagaraju (Ed.), Breaking tolerance to pancreatic cancer unresponsiveness to chemotherapy, Academic Press (Vol. 5).

Datkhile, K.D., Patil, S.R., Durgawale, P.P., Patil, M.N., Hinge, D. D., Jagdale, N.J., Deshmukh, V.N., More, A.L., 2021. Biogenic synthesis of gold nanoparticles using Argemone mexicana L. and their cytotoxic and genotoxic effects on human colon cancer cell line (HCT-15). J Genet. Eng. Biotechnol. 19, 1–11.

De Berardis, B., Civitelli, G., Condello, M., Lista, P., Pozzi, R., Arancia, G., Meschini, S., 2010. Exposure to ZnO nanoparticles induces oxidative stress and cytotoxicity in human colon carcinoma cells Toxicol. Appl. Pharmacol. 246, 116–127.

Delmas, J., Dalmasso, G., Bonnet, R., 2015. *Escherichia coli*: the good, the bad and the ugly. Clin. Microbiol. 4 (2).

Deshmukh, A.R., Gupta, A., Kim, B.S., 2019 (2019).. Ultrasound assisted green synthesis of silver and iron oxide nanoparticles using fenugreek seed extract and their enhanced antibacterial and antioxidant activities. BioMed. Res. Int.

Dutta, S., Sharma, S., Sharma, A., Sharma, R.K., 2017. Fabrication of core–shell-structured organic–inorganic hybrid nanocatalyst for the expedient synthesis of polysubstituted oxazoles via tandem oxidative cyclization pathway. ACS Omega 2, 2778–2791.

Gabrielli, B., Brooks, K., Pavey, S., 2012. Defective cell cycle checkpoints as targets for anti-cancer therapies. Front. Pharmacol. 3.

Ganji, P.N., Park, W., Wen, J., Mahaseth, H., Landry, J., Farris, A.B., Willingham, F., Sullivan, P.S., Proia, D.A., El-Hariry, I., 2013. Antiangiogenic effects of ganetespib in colorectal cancer mediated through inhibition of HIF-1α and STAT-3. Angiogenesis 16, 903–917.

Geinguenaud, F., Banissi, C., Carpentier, A.F., Motte, L., 2015. Iron oxide nanoparticles coated with a phosphorothioate oligonucleotide and a cationic peptide: exploring four different ways of surface functionalization. Nanomaterials 5, 1588–1609.

Hassan, D., Khalil, A.T., Saleem, J., Diallo, A., Khamlich, S., Shinwari, Z.K., Maaza, M., 2018. Biosynthesis of pure hematite phase magnetic iron oxide nanoparticles using floral extracts of Callistemon viminalis (bottlebrush): their physical properties and novel biological applications. Artif. Cells Nanomed Biotechnol. 46, 693–707.

Huang, L., Zeng, T., Xu, X., He, Z., Chen, J., Song, S., 2019. Immobilized hybrids between nitrogen-doped carbon and stainless steel derived Fe_3O_4 used as a heterogeneous activator of persulfate during the treatment of aqueous carbamazepine. Chem. Eng. J. 372, 862–872.

Iqbal, J., Abbasi, B.A., Ahmad, R., Shahbaz, A., Zahra, S.A., Kanwal, S., Munir, A., Rabbani, A., Mahmood, T., 2020. Biogenic synthesis of green and cost effective iron nanoparticles and evaluation of their potential biomedical properties. J. Mol. Struct. 1199, 126979.

Jagathesan, G., Rajiv, P., 2018. Biosynthesis and characterization of iron oxide nanoparticles using Eichhornia crassipes leaf extract and assessing their antibacterial activity Biocatal. Agric. Biotechnol. 13, 90–94.

Kajani, A.A., Bordbar, A.-K., 2019. Biogenic magnetite nanoparticles: a potent and environmentally benign agent for efficient removal of azo dyes and phenolic contaminants from water. J. Hazard. Mater. 366, 268–274.

Kędzierska, M., Potemski, P., Drabczyk, A., Kudłacik-Kramarczyk, S., Głąb, M., Grabowska, B., Mierzwiński, D., Tyliszczak, B., 2021. The synthesis methodology of PEGylated Fe_3O_4@ Ag nanoparticles supported by their physicochemical evaluation. Molecules 26, 1744.

Kim, J., Lee, K., Nam, Y.S., 2021. Metal-polyphenol complexes as versatile building blocks for functional biomaterials. Biotechnol. Bioproc E 26, 689–707.

Maddika, S., Ande, S.R., Panigrahi, S., Paranjothy, T., Weglarczyk, K., Zuse, A., Eshraghi, M., Manda, K.D., Wiechec, E., Los, M., 2007. Cell survival, cell death and cell cycle pathways are interconnected: Implications for cancer therapy. Drug Resist. Updat. 10, 13–29.

Madhuvilakku, R., Alagar, S., Mariappan, R., Piraman, S., 2017. Green one-pot synthesis of flowers-like Fe_3O_4/rGO hybrid nanocomposites for effective electrochemical detection of riboflavin and low-cost supercapacitor applications. Sens Actuators B Chem. 253, 879–892.

Madivoli, E.S., Kareru, P.G., Maina, E.G., Nyabola, A.O., Wanakai, S.I., Nyangau, J.O., 2019. Biosynthesis of iron nanoparticles using Ageratum conyzoides extracts, their antimicrobial and photocatalytic activity SN. Appl. Sci. 1, 1–11.

Mahmoudi, M., Simchi, A., Vali, H., Imani, M., Shokrgozar, M.A., Azadmanesh, K., Azari, F., 2009. Cytotoxicity and cell cycle effects of bare and poly(vinyl alcohol)-coated iron oxide nanoparticles in mouse fibroblasts. Adv. Eng. Mater. 11, B243.

Mahmoudi, R., Tajali Ardakani, M., Hajipour Verdom, B., Bagheri, A., Mohammad-Beigi, H., Aliakbari, F., Salehpour, Z., Alipour, M., Afrouz, S., Bardania, H., 2019. Chitosan nanoparticles containing Physalis alkekengi-L extract: preparation, optimization and their antioxidant activity. Bull. Mater. Sci. 42, 1–6.

Manju, S., Malaikozhundan, B., Vijayakumar, S., Shanthi, S., Jaishabanu, A., Ekambaram, P., Vaseeharan, B., 2016. Antibacterial, antibiofilm and cytotoxic effects of Nigella sativa essential oil coated gold nanoparticles. Microb. Pathog. 91, 129–135.

Meng, X., Lei, W., Yang, W., Liu, Y., Yu, Y., 2021. Fe_3O_4 nanoparticles coated with ultra-thin carbon layer for polarization-controlled microwave absorption performance. J. Colloid Interf. Sci. 600, 382–389.

Mohammed, N.K., Manap, A., Yazid, M., Tan, C.P., Muhialdin, B.J., Alhelli, A.M., Meor Hussin, A.S., 2016. The effects of different extraction methods on antioxidant properties, chemical composition, and thermal behavior of black seed (*Nigella sativa L.*) oil Evid.-based. Compl. Altern. Med.

Mortimer, C.J., Wright, C.J., 2017. The fabrication of iron oxide nanoparticle-nanofiber composites by electrospinning and their applications in tissue engineering. Biotechnol. J. 12, 1600693.

Nachmias, B., Ashhab, Y., Ben-Yehuda, D., 2004. The inhibitor of apoptosis protein family (IAPs): an emerging therapeutic target in cancer. Semin. Cancer Biol. 14, 231.

Namvar, F., Rahman, H.S., Mohamad, R., Baharara, J., Mahdavi, M., Amini, E., Chartrand, M.S., Yeap, S.K., 2014. Cytotoxic effect of magnetic iron oxide nanoparticles synthesized via seaweed aqueous extract. Int. J. Nanomed. 19, 2479.

Naseem, T., Farrukh, M.A., 2015,. Antibacterial activity of green synthesis of iron nanoparticles using Lawsonia inermis and Gardenia jasminoides leaves extract. J. Chem. 2015, 912342–912349.

Negut, I., Grumezescu, V., Ficai, A., Grumezescu, A.M., Holban, A. M., Popescu, R.C., Savu, D., Vasile, B.S., Socol, G., 2018. MAPLE deposition of *Nigella sativa*-functionalized Fe_3O_4 nanoparticles for antimicrobial coatings. Appl. Surf. Sci. 455, 513.

Noqta, O.A., Aziz, A.A., Usman, I.A., Bououdina, M., 2019. Recent advances in iron oxide nanoparticles (IONPs): synthesis and surface modification for biomedical applications. J. Supercond. Nov. Magn. 32, 779–795.

Rahman, S.S.U., Qureshi, M.T., Sultana, K., Rehman, W., Khan, M. Y., Asif, M.H., Farooq, M., Sultana, N., 2017. Single step growth of iron oxide nanoparticles and their use as glucose biosensor. Results Phys. 7, 4451–4456.

Rajan, A., Sharma, M., Sahu, N.K., 2020. Assessing magnetic and inductive thermal properties of various surfactants functionalised Fe_3O_4 nanoparticles for hyperthermia. Sci. Rep 10, 1–15.

Reddy, I.N., Sreedhar, A., Reddy, C.V., Shim, J., Cho, M., Kim, D., Gwag, J.S., Yoo, K., 2018. Enhanced visible-light photocatalytic performance of Fe_3O_4 nanopyramids for water splitting and dye degradation. J. Solid State Electrochem. 22, 3535–3546.

Saif, S., Tahir, A., Asim, T., Chen, Y., Adil, S.F., 2019. Polymeric nanocomposites of iron–oxide nanoparticles (IONPs) synthesized using Terminalia chebula leaf extract for enhanced adsorption of arsenic (V) from water. Colloid Interf. 3, 17.

Senthil, M., Ramesh, C., 2012. Biogenic synthesis of Fe_3O_4 nanoparticles using *Tridax Procumbens* leaf extract and its antibacterial activity on *Pseudomonas Aeruginosa*. Digest J. Nanomater. Biostruct. (DJNB) 7.

Shin, S.Y., Lee, Y., Park, J., Hwang, D., Jo, G., Lee, J.H., Koh, D., Lim, Y., 2018. Cell growth inhibitory effects of polyphenols with naphthalene skeleton against cisplatin-resistant ovarian cancer cells. Appl. Biol. Chem. 61, 697–701.

Siddiqui, S.I., Zohra, F., Chaudhry, S.A., 2019. *Nigella sativa* seed based nanohybrid composite-Fe_2O_3–SnO_2/BC: a novel material for enhanced adsorptive removal of methylene blue from water. Environ. Res. 178, 108667.

Stark, W.J., Stoessel, P.R., Wohlleben, W., Hafner, A., 2015. Industrial applications of nanoparticles. Chem. Soc. Rev. 44, 5793–5805.

Sundaram, P.A., Augustine, R., Kannan, M., 2012. Extracellular biosynthesis of iron oxide nanoparticles by Bacillus subtilis strains isolated from rhizosphere soil. Biotechnol Bioproc. E17, 835–840.

Sung, H., Ferlay, J., Siegel, R.L., Laversanne, M., Soerjomataram, I., Jemal, A., Bray, F., 2020. Global cancer statistics, 2020 Globocan estimates of incidence and mortality worldwide for 36 cancers in 185 countries. CA: A Cancer J. Clin.

Tang, S., Zhao, M., Yuan, D., Li, X., Wang, Z., Zhang, X., Jiao, T., Ke, J., 2021. Fe_3O_4 nanoparticles three-dimensional electro-peroxydisulfate for improving tetracycline degradation. Chemosphere 268, 129315.

Tara, N., Siddiqui, S.I., Nirala, R.K., Abdulla, N.K., Chaudhry, S.A., 2020. Synthesis of antibacterial, antioxidant and magnetic *Nigella sativa*-graphene oxide based nanocomposite BC-GO@Fe_3O_4 for water treatment. Colloid Interf Sci. Commun. 37, 100281.

Wang, X., Liu, Y., Arandiyan, H., Yang, H., Bai, L., Mujtaba, J., Wang, Q., Liu, S., Sun, H., 2016. Uniform Fe_3O_4 microflowers hierarchical structures assembled with porous nanoplates as superior anode materials for lithium-ion batteries. Appl. Surf. Sci. 389, 240–246.

Whitfield, P., Mitchell, L., 2004. X-ray diffraction analysis of nanoparticles: recent developments, potential problems and some solutions. Int. J. Nanosci. 3, 757–763.

Yew, Y.P., Shameli, K., Miyake, M., Kuwano, N., Khairudin, N.B.B. A., Mohamad, S.E.B., Lee, K.X., 2016. Green synthesis of magnetite (Fe_3O_4) nanoparticles using seaweed (*Kappaphycus alvarezii*) extract. Nanoscale Res. Lett. 11 (1), 1–7.

Youhannayee, M., Nakhaei-Rad, S., Haghighi, F., Klauke, K., Janiak, C., Ahmadian, M.R., Rabenalt, R., Albers, P., Getzlaff, M., 2019. Physical characterization and uptake of iron oxide nanoparticles of different prostate cancer cells. J. Magn. Magn. Mater. 473, 205–214.